Extreme Mechanics Letters 77 (2025) 102323

Contents lists available at ScienceDirect

Extreme Mechanics Letters

journal homepage: www.elsevier.com/locate/eml

Brittle fracture of ultrathin gold nanosheets induced by local phase change and energy dissipation

Jieun Park [a,1,2], Guh-Hwan Lim [b,1], Dayoung Yoo [a,3], Tae-Hoon Kim [c], Jong-Man Kim [a,d], Cheol-Woong Yang [b], Joonkyung Jang [a,d], Yoon Suk Choi [e], Byunkwon Lim [b,*], Jeffrey W. Kysar [f,*], Dongyun Lee [a,d,**]

[a] Department of Nano Fusion Technology, Pusan National University, Busan 46241, Republic of Korea
[b] School of Materials Science and Engineering, Sungkyunkwan University (SKKU), Suwon 16419, Republic of Korea
[c] Department of Materials Science & Engineering, Chonnam National University, Gwangju 61186, Republic of Korea
[d] Department of Nanoenergy Engineering, Pusan National University, Busan 46241, Korea
[e] School of Materials Science and Engineering, Pusan National University, Busan 46241, Korea
[f] Department of Mechanical Engineering, Columbia University, New York, NY 10027, USA

ARTICLE INFO

Keywords:
Au nanosheet
Fracture
Phase transformation
Nanoindentation
Molecular dynamics simulations

ABSTRACT

Metals with a face-centered cubic (*fcc*) structure, such as gold (Au), are generally known for their excellent ductility. However, in this study, we observed a novel brittle fracture behavior in ultrathin Au nanosheets with a thickness of approximately 15 nm and a diagonal length of up to 80 μm, synthesized via an aqueous solution method. Nanoindentation experiments on these nanosheets revealed a unique fracture pattern, characterized by crack propagation at angles of 120° from the indentation point. Molecular dynamics (MD) simulations replicated this unusual behavior, attributing it to a localized phase transformation from the *fcc* to hexagonal close-packed (*hcp*) structure under external stress. We hypothesize that this phase transition is initiated by stacking faults introduced during the nanosheet fabrication process. The observed brittle fracture is further influenced by an energy dissipation mechanism, as evidenced by the formation of slip lines around the fracture site. Our findings suggest that even in ductile metals like Au, brittle fracture can occur due to localized phase changes and energy dissipation. This study provides new insights into the mechanical behavior of ultrathin Au nanosheets, with implications for their application in nanoelectronics and other advanced technologies.

1. Introduction

Anisotropic gold (Au) nanostructures, particularly ultrathin large-area nanosheets, have attracted significant attention as potential building blocks for nanoelectronic devices, including energy harvesting systems and strain sensors [1–5]. In this study, the ultrathin Au nanosheets were synthesized via the reduction of aqueous Au salt solutions, resulting in structures with a thickness of less than 20 nm and lateral dimensions up to 2000 μm^2. The controlled synthesis of such nanosheets provides a pathway for creating high-performance Au thin films that can serve as efficient conductive layers or active surfaces in nanoelectronic and optoelectronic devices. In particular, we aim to apply these materials in flexible electronic systems where mechanical compliance and durability are essential. Understanding the mechanical behavior of these Au nanosheets is crucial, as their mechanical properties directly affect the performance and lifespan of flexible devices [6]. Furthermore, investigating their behavior at the nanoscale offers valuable insights into the intrinsic mechanical properties of gold in low-dimensional forms.

Au is traditionally considered one of the most ductile metals; however, at room temperature, there have been rare instances where its ductility is significantly reduced, leading to cracking. Such cases have seldom been reported [7], even on the nanoscale. Recently, Wang et al.

* Corresponding authors.
** Corresponding author at: Department of Nanoenergy Engineering, Pusan National University, Busan 46241, Korea.
E-mail addresses: blim@skku.edu (B. Lim), jk2079@columbia.edu (J.W. Kysar), dlee@pusan.ac.kr (D. Lee).
[1] J. P. and G. L. contributed equally to this work
[2] Current address: Samsung Electro-mechanics Co., Ltd., Busan 46754, Republic of Korea
[3] Current address: Institute of Advanced Composite Materials, Korea Institute of Science and Technology, Jeonbuk 55324, Korea

https://doi.org/10.1016/j.eml.2025.102323
Received 3 January 2025; Received in revised form 31 March 2025; Accepted 2 April 2025
Available online 4 April 2025

[8] demonstrated that under certain conditions, Au atoms can adopt a hexagonal close-packing (hcp) stacking sequence, forming a material that exhibits brittle fracture in Au nanowires. Building on these observations, we demonstrate here for the first time that brittle fracture can also occur in ultrathin Au nanosheets. This testing methodology is not entirely new and has previously been applied to other 2D materials such as MoS_2 and graphene, as well as to sputtered polycrystalline copper films on carbon grids [9–12]. Such comparisons are crucial as they not only validate our testing approach but also provide a broader perspective on the mechanical behavior of ultrathin materials under similar conditions.

Stacking faults, such as a *hcp* (a structure where atoms are packed together in a hexagonal arrangement, with layers alternating to achieve the closest possible packing) stacking sequence in *fcc* (a crystal structure where atoms are located at each corner and the centers of all the cube faces of a unit cell) crystal structure, may be related to a low stacking-fault energy of Au [7]. The mechanical properties of ultrathin Au nanosheets may be altered by involvement of structural defects, but have not been studied, neither theoretically nor experimentally. In addition, we intend to interpret the results of this study by using the analysis of the process of fracture in a competition between energy dissipation mechanisms [13,14].

In the case of ultra-thin nanomaterials including two-dimensional structures, mechanical properties can be quantitatively analyzed using nanoindentation or atomic force microscopy (AFM). It is made in such a way that an approximate in-plane load can be applied to an ultra-thin nanomaterial placed on a perforated substrate. Accordingly, this analysis often demands a specimen with a sufficiently large lateral size to cover a hole of a few micrometers in diameter. In this study, we synthesized and used ultrathin Au nanosheets with a lateral size of tens of micrometers and a thickness of ~20 nm or less using the previously reported hydrothermal process [4,5]. Deformation and fracture behavior of the nanosheets were investigated by using a nanoindentation method (G200™, KLA Corp. USA). The brittle fracture accompanying the formation and propagation of three cracks with a divergent angle of 120° was observed in Au nanosheets. There may be differences in the stress distribution depending on the shape of the indenter tip. To take this effect into consideration, three tip shapes were used. Detailed experimental procedures are in supplementary material.

In the next two sections, the microstructure and mechanical behavior of Au nanosheets will be discussed in detail. Recently, studies have been published to explain the ductile-brittle transition of ductile *fcc* structured materials which is caused by phase transition. Lu et al. [7] reported that due to the relatively low stacking fault energy of Au and the collective motion of Shockley partial dislocations $\frac{<112>}{6}$ along *{111}* slip planes, twins easily form. This formation significantly affects the mechanical behavior of nanoscale Au [15,16]. According to Lu et al. [7], misalignment occurring between the nanowire and the tensile axis inevitably leads to shear along the transverse plane. This acts as the cause of the stacking faults and can provide a driving force that subsequently causes twins. And interestingly, it has been reported that the crystal structure of Au can be transformed from *fcc* to *hcp* and *vice versa*, which can also be converted under the influence of twins associated with stacking fault [17–19].

In this study, we propose several possible scenarios to understand the brittle fracture behavior of ductile gold in anisotropic nanosheets and provide experimental evidence to support these findings. The concepts of stacking faults that may occur during the synthesis of gold nanosheets, the possibility of local phase transformations due to external stress concentration, and energy dissipation mechanisms should be considered in understanding the novel mechanical behavior of ultra-thin Au nanosheets.

2. Experimental section

2.1. Fabrication and transferring of Au nanosheets

In the typical synthesis of Au Nanosheets (NSs), 5 mL of an aqueous solution containing 1.7 mg of L-arginine (Sigma Aldrich) was placed in a 20-mL vial at room temperature before heating the solution to 95 °C. Meanwhile, 2 mL of aqueous solution containing 13.5 mg of hydrogen tetrachloroaurate trihydrate ($HAuCl_4 \cdot 3\,H_2O$, Alfa Aesar) was drop-injected into the L-arginine solution using a pipette. The reaction mixture was maintained at 95 °C for 2 h and then cooled down to room temperature. The solvent was then removed using a pipette. The final solution was then prepared by mixing with ethanol/distilled water, after which the Au NSs precipitated. Then, the Au NSs was transferred onto SiO_2 substrates with 10-μm-diameter holes for the nanoindentation tests.

An oxidized silicon (SiO_2) substrate was cleaned using a piranha solution. A ~1.4-μm-thick photoresist (PR) was then spin-coated on the cleaned substrate and patterned via a standard photolithography process. The silicon dioxide layer was then selectively etched by dipping it in a buffered oxide etchant at room temperature. After removing the PR etching mask, a silicon trench with 10 μm diameter was formed by vertically etching the exposed silicon part via a deep reactive ion etching process.

2.2. XRS, SEM, TEM and AFM measurements

The crystal structures and microstructures of Au nanosheets were analyzed by XRD, SEM, EBSD, AFM, and TEM. To observe and measure the surface morphology and size of Au nanosheets on the Si wafer, SEM and AFM analyses were used. The crystallinity of Au nanosheets was measured using XRD, for which Au nanosheets were transferred on Si wafer several times to form a thick layer to obtain sufficient XRD data. In addition, the lattice structure of the sample was examined by TEM.

After indentation, the surfaces of indented sample were also investigated by SEM and TEM. The mechanical behavior of Au nanosheets was confirmed from SEM and TEM data. Figure S1 is an SEM image of Au nanosheets mounted on a perforated SiO_2/Si substrate. As mentioned in the text, the triangular and hexagonal Au nanosheets are well formed and can be seen extending over the hole. The thickness of Au nanosheets was measured using AFM. As shown in Fig. S2, the thickness is about 20 nm and the entire sheet has a uniform thickness. It can be seen that it is placed evenly on the hole even after transfer (Fig. S2 (b))

2.3. Nanoindentation test

For the nanoindentation experiment, a Nanoindenter G200™ nanoindentation system (KLA Corp. USA) was used, and a Dynamic Contact Module (DCM™) load cell was employed, which provides higher resolution compared to that of the XP™ load cell. There may be differences in the stress distribution depending on the shape of the indenter tip. To take this effect into consideration, three tip shapes were used. Basically, experiments were conducted using Berkovich tips, and indentation experiments were conducted using cube-corner and conical tips to confirm the fracture pattern. The indentation depth was in the range of ~50–500 nm with a loading rate of 0.075 mN/s applying the same load over time to the specimen in the constant strain rate, 0.05/s. To determine the intrinsic behavior of the Au nanosheets, the samples were transferred onto Si substrates with 10-μm-diameter holes arranged at 5-μm intervals, and the indentation tests were carried out in a free-standing position. After indentation, the surfaces of the indented samples were investigated by SEM and TEM. The mechanical behavior of the Au nanosheets was confirmed based on the SEM and TEM data.

2.4. Molecular dynamics (MD) study

Molecular dynamics was performed to simulate the behavior of the atoms when external forces were applied to the Au NSs. It was assumed that Au atoms were stacked with 8 layers in the closest packing, and the Au geometry was taken to be a circle with a diameter of 20 nm (Fig. S6). Herein, the interatomic spacing was set for 2.88 Å for the *fcc* structure and 2.96 Å for the *hcp* structure based upon literature values [8]. We set the simulation box size as $L_x = L_y = 24$ nm and $L_z = 4$ nm. An external force ranging from 0 to 0.112 nN/atom was applied in the vertical direction of the Au sheets. The external force was exerted only on the Au atoms within a 1 nm radius circle from the center of the sheet. The interatomic interaction of Au atoms was modelled by using the embedded atom model (EAM) potential. We simulated the behavior of the atoms for 500 ps with a 2 fs timestep at 300 K. These simulations were performed in the NVT ensemble by using the Nosé-Hoover thermostat [20,21]. All MD simulations have been performed by using Large-scale Atomic/Molecular Massively Parallel Simulator (LAMMPS) [22] and visualized by using Visual Molecular Dynamics (VMD) [23].

3. Results and discussion

3.1. Microstructures and crystallinity of ultrathin Au nanosheets

The as-synthesized ultrathin Au nanosheets had a hexagonal or truncated triangular shape, and their diagonal sizes ranged up to 80 μm (Fig. 1 & S1). A brief description of the crystallographic observation of the Au nanosheets used in this study is as follows: In the transmission electron microscopy (TEM) analysis, a selected area electron diffraction (SAED) pattern taken from an Au nanosheet was composed of diffraction spots with a 6-fold rotational symmetry (Fig. 1), indicating that its top and bottom faces are enclosed by *{111}* planes.

The results of TEM and X-ray diffraction (XRD) analysis are shown in Fig. 1, where Fig. 1(a) is of morphologies of the nanosheets and Fig. 1(b) is of cross-sectional views of the ultrathin Au nanosheets. The thickness of the Au nanosheets shown in Fig. 1(b) is about 15 nm and most of them are less than 20 nm. As shown in Fig. S2, the thicknesses were also confirmed by AFM, which were uniform regardless of the size of Au nanosheets. The distance measured between the two planes stacked in the thickness direction was ~0.24 nm shown in Fig. 1(b). Fig. 1(c) shows the Bragg reflection patterns on the zone axis *[111]*. As shown in the pattern, *{220}* intense spots and $\frac{1}{3}${422} weak spots are visible. Observation of the extra spots associated with $\frac{1}{3}${422} diffractions presents various possibilities for interpreting crystal structures: the presence of twin planes and/or stacking faults in the *{111}* plane and local *hcp* crystal structure in Au nanosheet [24–26]. It should be noted that Cayron et al. [27] also asserted that the $\frac{1}{3}${422} diffraction should not be related to the hcp phase in Si nanowire studies. The cross-sectional, high-resolution TEM (HRTEM) images of the Au nanosheets confirmed the presence of such defects parallel to their top and bottom faces. Insets of Fig. 1(b) showed that Fast Fourier transform (FFT) patterns, and twins are clearly observed. However, these twins and stacking faults are not always observed in TEM work (see Fig. S3). The X-ray patterns of Au nanosheets shown in Fig. 1(d) indicate that the Au sheets grew as a close-packed single crystal oriented in *(111)*, and this result can also be seen in the TEM diffraction pattern shown in Fig. 1(c). Therefore, it was found that the close-packed surface of the Au atoms was aligned perpendicular to the *[111]* direction in the z-axis and faced toward the $< 110 >$ direction shown in the inset of Fig. 1(d).

As known from the literature (calculated or experimental), the lattice parameter of Au in *fcc* structure is approximately ~4.0786 Å, and the lattice parameters ***a*** and ***c*** of *hcp* Au are approximately 2.96 Å and 4.84 Å, respectively [8]. In this study, the in-plane interatomic spacing for the *fcc* Au structure was geometrically calculated as 2.88 Å based on the lattice parameter of 4.0786 Å, and the in-plane interatomic distance for the *hcp* Au structure was chosen as 2.96 Å according to the literature value [17]. These values were chosen for the molecular dynamics (MD)

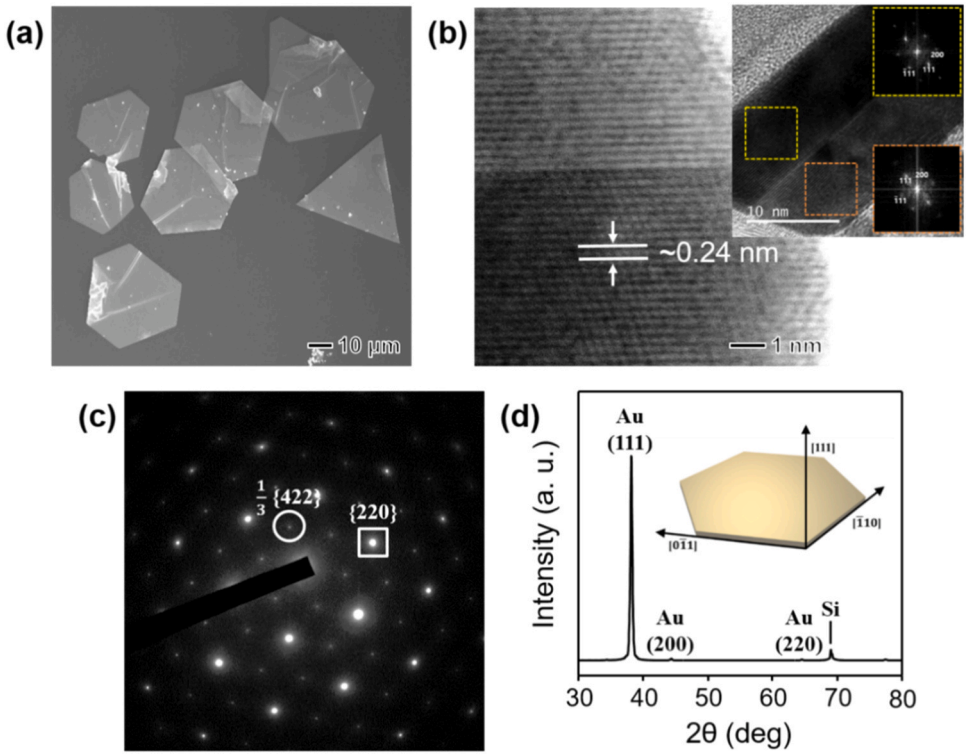

Fig. 1. Morphology and crystal structure of the Au nanosheets: (**a**) FE-SEM image of Au NSs; (**b**) cross-sectional view HRTEM and TEM & FFT patterns of the Au nanosheets; (**c**) *{220}* intense spots (squared) and $\frac{1}{3}${422} weak spots (circled) of Bragg reflections in the *[111]* zone axis; (**d**) XRD patterns and schematic illustration of the Au nanosheets.

simulation to intentionally maximize the differences in parameters between the *fcc* and *hcp* structures of Au.

The selected area electron diffraction (SAED) pattern in the TEM study also confirmed that Au nanosheets were single crystalline materials with *fcc* structure, as shown in Fig. 1(C). All diffraction patterns can be commonly identified as *fcc* structures. As shown in Fig. 1(C), intense *{220}* reflections (open square) are clearly observed and very weak reflections of $\frac{1}{3}$ *{422}* patterns are also detected, which the open circle indicates the reflection. Owing to the appearance of $\frac{1}{3}$ *{422}* reflection patterns it can be presumed that the structure of the Au nanosheets used in this study is not perfectly *fcc* because these reflection patterns are generated by the stacking faults [26,28]. The inset of Fig. 1(d) shows a schematic diagram of the crystallographic orientations of Au nanosheets based on XRD and TEM studies.

3.2. Novel mechanical behavior of the ultrathin Au nanosheets

For the nanoindentation test, ultrathin Au nanosheets were transferred onto a SiO_2 substrate. Fig. 2 shows a scanning electron microscope (SEM) image of a transferred Au nanosheet with an array of cylindrical holes each with diameter of 10 μm and depth of 10 μm. The sizes of the triangular or hexagonal Au nanosheets varied from several to tens of micrometers (refer Fig. S1). Fig. 2(a) shows a representative image of Au nanosheets after the nanoindentation tests with Berkovich tip (a three-sided pyramid diamond tip with the same area-to-depth ratio as a traditional Vickers indenter, centerline-to-face angle of 65.3°). As shown in Fig. 2(a), the nanoindentation test was performed on the material suspended over holes (indicated by white circles) in an Au nanosheet having a size of about 65 μm from a hexagonal surface to a surface. Since the size of the Au nanosheets was sufficiently large to cover several holes, nanoindentation tests could be performed several times on the same Au nanosheets. Similar radial crack formation has been investigated in brittle materials under impact loading [29], yet our study shows that such patterns can also emerge from localized phase transitions and stress dissipation in quasi-static conditions.

After the nanoindentation tests with Berkovich tip, three cracks with a divergent angle of 120° were observed and cleavage fractures appeared in the Au nanosheets, which can typically be observed in brittle materials. Load-displacement curves presumed to show the cracking phenomenon can be seen in Fig. S4. To see if the shape of the Berkovich tip affects the angle of the crack, we intentionally made a large indentation mark to compare the direction of the crack with the shape of the Berkovich tip. The black rectangle inset in Fig. 2(a) is an enlargement of the designated region, and the edge of the Berkovich tip is indicated by a solid black line. Figs. 2(b) and 2(c) are enlarged images of the white dotted circle in Fig. 2(a) and white rectangle in Fig. 2(b), respectively. The comparison of the directions of cracks and tip edges shown in Figs. 2(b) and 2(c) clearly indicates that the Berkovich tip edges and cracks are not matched. Thus, the directions of the cracks are independent of the tip geometry.

To examine whether the shape of the indenter tip influences fracture behavior, experiments were conducted using a cube-corner tip, a conical tip, and a Berkovich tip. It was observed that the fracture behaviors with the cube-corner and conical tips were similar to those with the Berkovich tip, indicating that the shape of the indenter tip does not significantly affect the fracture behavior of the Au thin film. Fig. 3(a) in the supporting information shows the cube-corner tip and provides additional insights into fracture behaviors observed during indentation. Figs. 3(b) and 3(c) depict indentation with conical and Berkovich tips, respectively, where the dashed lines indicate the same divergent angles across the different tips. Notably, Fig. 3(b) illustrates a unique fracture mode observed in the molecular dynamics (MD) simulation under a slightly higher load of 0.08 nN/atom compared to that shown in Fig. 5 (b). In the case of the conical tip, the fracture behavior was found to be brittle, similar to that observed with the Berkovich tip (Fig. 3(c)). The dotted lines in Fig. 3(b) and Fig. 3(c) (reconstructed from Fig. 2) indicate the same divergent angle, further supporting the similarity in fracture behavior. Interestingly, Fig. 3(b) reveals another failure mode in the MD simulation under the slightly higher load, emphasizing that a more concentrated load is typically applied in the case of a conical indenter.

The white arrows shown in Fig. 2(c) indicate plastic slip lines that occurred around the cracks during nanoindentation tests. The direction in which the slip lines occurs coincides with the edge direction of the Au nanosheets (compare with face of hexagonal Au nanosheets in Fig. 2(a) and arrows '***a***', '***b***', and '***c***' in Fig. 2(c)) as well as between cracks and slip lines are 60° apart. It can be determined that the cracks occurred along the overlapping parts of the slip lines. In other words, it seems that '$\boldsymbol{c}'$' cracks occurred along the points where slip lines '***a***' and '***b***' meet, and the rest are thought to be formed in the same way. The formation and propagation of cracks will be comprehensively explained later using a schematic diagram along with the simulation results. In addition, it can be observed that the slip line formed on the Au nanosheets subjected to point loading with an indenter and the direction of crack propagation are quite similar. As a result of checking by electron backscattering

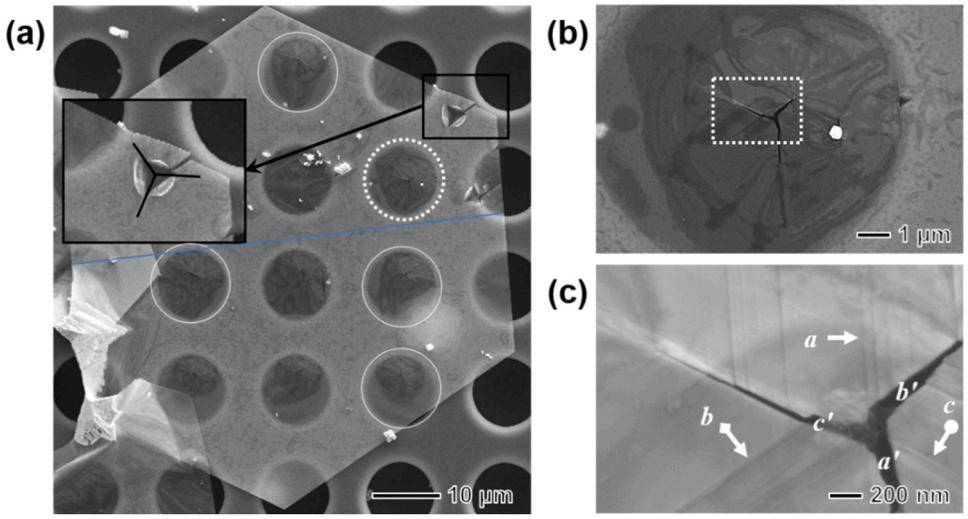

Fig. 2. Scanning electron micrograph of large-area Au nanosheets on the SiO_2 hole substrate where the indentation experiment was conducted: (a) Electron micrograph of indented Au nanosheets and indenter shape; (b) Enlarged image of the white dashed circle in (a); (c) Enlarged image of the white dashed rectangle in (b) and cracks and slip lines.

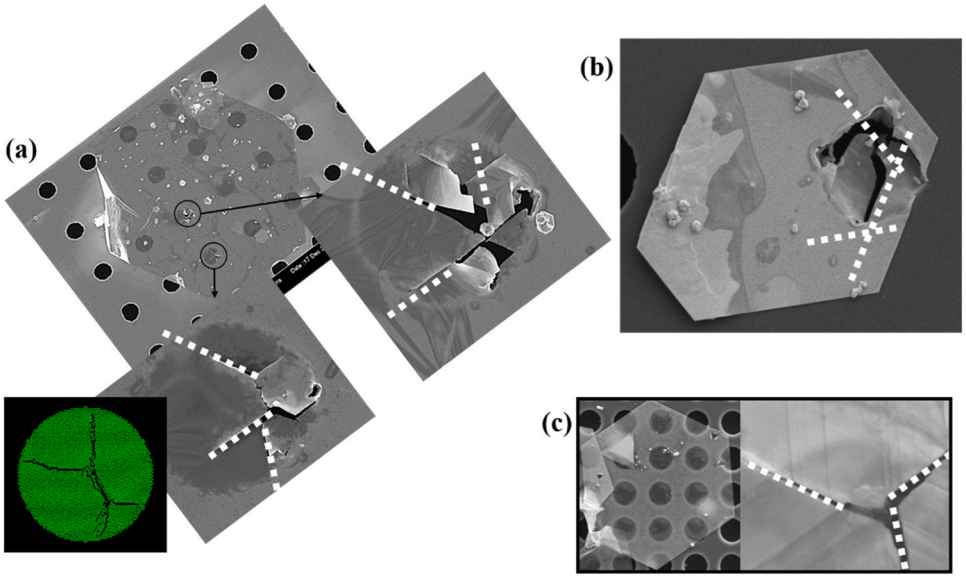

Fig. 3. Fracture behaviors during indentation with (a) cube corner tip; (b) conical tip (ϕ=50 nm); and (c) Berkovich tip for reference.

diffraction (EBSD), it can be seen that it is in the $< 110 >$ direction, which is shown in Fig. 4. Fig. 4(a) shows an EBSD mapping of the rectangular region in Fig. 4(b). Besides, cracks '$\boldsymbol{b}'$ ' and '$\boldsymbol{c}'$ ' are not accurately identified in the EBSD image because the nanosheets protrude out of the plane during retraction of the indenter after indentation and remain as shown in Fig. 4(a). The crack in the '$\boldsymbol{a}'$ ' direction shows enough data to interpret the crystallographic direction of cracks with green pixels near cracks as seen in the EBSD map. This is matched with the non-tilting plane image, and the crack direction is $< 110 >$. For *fcc* crystal structures, all *h*, *k*, and *l* need to be either even or odd (mixed indices need to be absent in diffraction peaks); however, as shown in Fig. 4(a), the existence of a mixed index such as the *(112)* plane is estimated to be due to the formation of other crystal structures or crystal defects in part of *fcc* due to the press-in load. This transformation can be hypothesized as the cause of brittle fracture of Au nanosheets. We believe that the change in the *fcc* crystal structure to an *hcp*-like structure i.e., partially *hcp* packing sequence, either due to the localized indenting load or stacking sequence changing due to cross-over slip lines, can be a dominant factor in the formation of cleavage fractures.

Lu et al. [7] studied the fracture behavior of sub-20-nm gold wires and they reported the observation of two different phenomena: ductile and brittle-like fracture behaviors. The ductile fracture behavior is typical of *fcc* materials, such as Au and Ag; however, the brittle-like fracture behavior is abnormal. Lu et al. suggested that the formation of twins during the deformation can result in a phase transformation from *fcc* to *hcp* crystal structure, which results in an atypical brittle-like fracture in *fcc* materials. The tensile stress was ~1 GPa, and the Young's modulus stated in the literature ranges from ~25–28 GPa in the case of brittle-like fracture.

During the indentation of Au nanosheets, dislocations were generated around indentation tip, and these dislocations are known to move through the motion of the partial dislocations in the $< 112 >$ direction on the {111} plane. During the motions, the stacking sequences of *fcc* Au (ABCABCA…) can be matched with the stacking sequence of *hcp* Au (ABABA…) [17], and then, the brittle fracture can occur at the points satisfying the requirements of failure. MD simulations (the conditions for MD simulation are detailed in the supporting information shown in Fig. S5, S6) were performed to understand the unique behavior and to verify our assumption to reach the fracture of Au nanosheets by the nanoindentation test.

Interestingly, while lowering the stacking fault energy in FCC metals generally increases ductility - as observed in many FCC concentrated solid solution alloys (e.g., in references [30,31]) - our results revealed brittle fracture behavior in ultrathin Au nanosheets, both experimentally and through simulation. Notably, when we assumed an HCP crystal structure in the simulation, brittle fracture behavior was successfully reproduced. These findings suggest that a local phase transition from FCC to HCP may occur during indentation at the nanoscale, resulting in the observed brittle behavior.

The results of MD simulations, shown in Fig. 5(a), indicate that no significant cracks occur when indentation is performed on the *fcc* crystal structure. When the load is increased, deformation occurs when the force reaches 0.112 nN/atom, and the sheet is pierced in the part where the load is applied. No propagation of the cracks such as observed

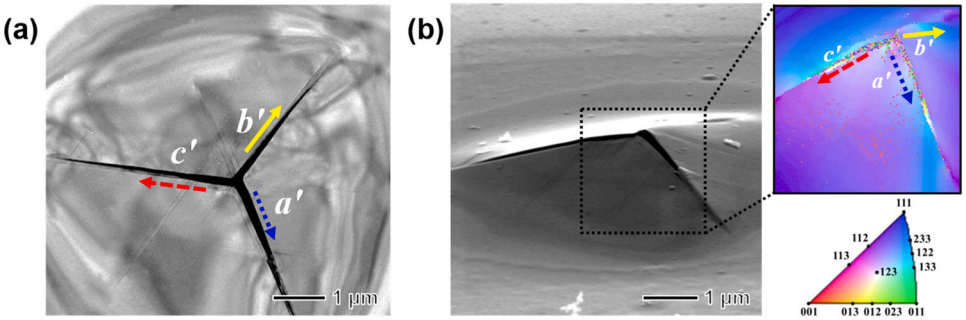

Fig. 4. EBSD analysis of the indented Au NS: (a) Plane view SEM image of the cracks of the indented Au nanosheets; (b) SEM image at and EBSD maps tilted at 70° of the indented Au nanosheets. Green pixels near crack $\boldsymbol{a}'$ indicating $< 110 >$ direction that was analyzed by EBSD.

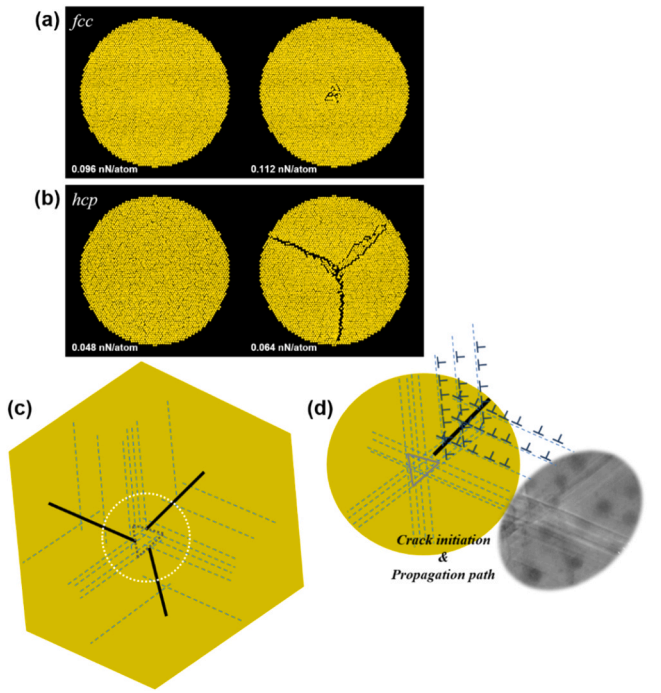

Fig. 5. Molecular Dynamics simulation data for the Au nanosheets with (A) *fcc*; (B) *hcp* structure; (C) schematic of the indentation and slip line formed on the nanosheets; (D) schematics for formation and tangling of dislocation on Au nanosheets.

experimentally was predicted by this simulation. In the case of the *hcp* crystal structure, it can be seen that as the load increases, the same radial cracking of 120 ° as observed in the experiment occurs (side views are in Fig. S6). The force that formed the radial cracks in the *hcp* structure was approximately twice smaller than the force puncturing the *fcc* crystal structure. It can be assumed that stress concentrations at the localized *hcp* structures due to the stacking fault in the Au nanosheets and cracks are directly initiated and propagated along those defects.

Fig. 5(c) is a schematic diagram of the cracks and slip lines in the indentation of the ultrathin Au nanosheets in Fig. 2(a). Fig. 5(d) is an enlarged part of the white circle in Fig. 5(c), and it is expressed that the slip lines are concentrated on the loading part, which can be confirmed in the actual SEM image (before crack initiated) on Fig. 5(d). The schematic diagram drawn in the middle of Fig. 5(d) represents the increase in dislocation density as the slip lines overlap. It is thought that this increase in dislocation density creates the necessary conditions for cracking to occur.

Kysar [13,14] presented a framework to evaluate the competition between cleavage, crack tip dislocation nucleation, and Frank-Read (FR) dislocation source activation near the crack tip as potential energy dissipation mechanisms. If the FR source is generated easier than other two possible phenomena, it can be said that it has extrinsically ductile characteristics. If the cleavage occurs at a lower load than the crack tip dislocation nucleation, the material was judged to have intrinsically brittle properties. On the other hand, if the crack tip dislocation nucleation was dominant at the lower load, the material was judged to be intrinsically ductile. Kysar interpreted the above three energy dissipation mechanisms to operate competitively, and the fracture behavior of the material changes depending on which mechanism prevails. In the graph of the reference [13], the ductile-dominant region and the brittle characteristic dominant region were defined using the two dimensionless parameters, $b\rho_{disl}^{\frac{1}{2}}$ (where b is the Burgers vector and ρ_{disl} is the dislocation density) and τ_p/μ (where τ_p is the Peierls stress and μ is the elastic shear modulus), and the ductile-brittle transition model was presented according to the change of the two parameters.

Applying those concepts to the experiments and simulations in this study, we note that in specimens with nanometer scale thickness that FR dislocation nucleation is unlikely due to the paucity of pre-existing dislocations. Therefore, such materials are not expected to be extrinsically ductile. Thus, the operative energy dissipation mechanism is between crack tip cleavage and crack tip dislocation nucleation. It is apparent from the experiments that dislocations are nucleated as the crack tip propagates through the material, so this material would be classified as being intrinsically ductile according to the criterion of Rice and Thomson [32]. Nevertheless, since FR sources are not activated away from the crack tip the overall material behavior is brittle.

Another possible mechanism leading to the creation of cracks in this ultrathin Au nanosheets is phase transformation under high pressure and/or high-input energy by indentation. Diao et al. [33] reported that gold nanowire with *fcc* structure was transformed into body-centered tetragonal (*bct*) structure by surface stress. Due to the change of the lattice structure, the mechanical properties of the Au nanosheets changed from ductile to brittle. However, there is not sufficient evidence for this phenomenon, thus, further studies need to be performed.

3.3. Measurement of the elastic properties of the ultrathin Au nanosheets

Extensive research has been conducted to understand plates and membranes; however, it is difficult to find a suitable theoretical description for the properties of a given film, such as thickness, span, pre-strain, and elastic properties. Komaragiri et al. [34] provided maps based on boundary layer analysis, to understand the mechanical behavior of the film. Wan et al. [35] also presented an important approach for the description of thin clamped circular film. Kysar and Hone research groups suggested a semi-empirical relationship between the force and displacement of indentation of a free-standing circular membrane from which the elastic stiffness of 2D materials can be determined by fitting against the experimental data [9,10] assuming isotropic mechanical response, which can also be extended to thin films with thickness within tens of nm that can be treated as membranes. We performed a nanoindentation test on the Au nanosheets to characterize the mechanical properties, and the initial section of loading curve has been fitted with the semi-empirical equation [9]

$$F = \sigma_0^{2D} \bullet \pi \bullet \delta + E^{2D} \bullet q^3 \bullet \frac{1}{a^2} \bullet \delta^3 \quad (1)$$

where F is the applied force, δ is the deflection at the center point, σ_0^{2D} is the pretension in the film, E^{2D} is the elastic modulus of the thin film, and $q = 1/(1.05 - 0.15\nu - 0.16\nu^2) = 1.04$ is a dimensionless constant, where ν is the Poisson's ratio taken as 0.415 [36]. The result of the fitting is shown in Fig. 6. As mentioned above, Eq. 1 is a reasonable approximation to describe extremely thin structures, such as 2D materials. Recent studies to further address the mechanics of the relationship between force and displacement include [37,38], as discussed in the

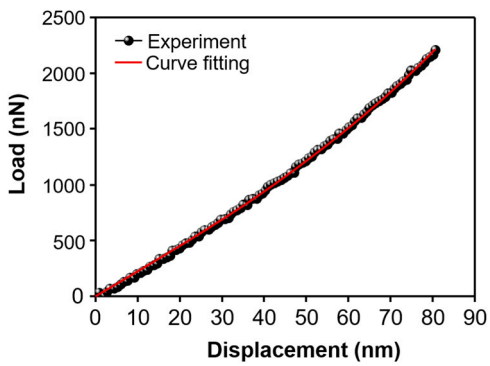

Fig. 6. Initial section of the load–displacement curve of the Au nanosheets and curve fitting to the equation in references [9,10].

Supplementary Information. We estimated that a pretension of approximately 7 N/m was applied to the Au nanosheet, which was obtained by fitting the experimental data using Eq. (1).

We obtained values describing the mechanical properties of 2D sheets in using Eq. 1. The quantities used in Eq. 1 could be applied for three-dimensional (3D) parameters by the division by the interlayer spacing in the Au nanosheet, which was ~0.24 nm measured by high-resolution transmission electron microscopy (HRTEM). As mentioned, these quantities cannot be used to predict further mechanical properties because they are not intrinsic properties of a single sheet [9,10]. Nevertheless, we obtained an elastic modulus value of 30 GPa for the nanosheet using Eq. 1, which is similar to the literature value [7].

In addition, it is possible to estimate the maximum total strain suffered by the membrane immediately below the indenter tip based on analyses by [39,40]. Equation 17 of reference [40] suggests that at a loading of 2.25 μN with an indenter tip with 40 nm radius that the sum of the prestrain and the in-plane strain induced by the indentation process is about 0.034 of which about 0.016 is from the prestrain. Therefore, the analysis of the force vs. indentation depth data in Fig. 6 is sufficient to sample the elastic properties of the membrane.

Due to the stacking fault occurring during the synthesis process, the *fcc* structure was partially transformed into an *hcp* structure, and as the ability of the *hcp* structure to withstand the stress by nanoindentation is lower, cracks initiated and propagated in the thin film. Wang et al. [8] reported calculated values for the shear modulus (G) of Au according to the Voigt [41], Reuss [42], and Hill [43], which are 19.5 GPa for *hcp* Au and 26.8 GPa for *fcc* Au. Interestingly, the Young's modulus of Au nanosheets calculated in this study is similar to the shear modulus described in the study by C. Wang et al. [8]. It is presumed that the Young's modulus and the shear modulus of 2D materials and ultrathin materials are not distinguishable due to the directions of the stresses, which are almost only in-plane for the materials. C. Wang et al. also reported the bulk modulus (B) of Au in two different crystal structures, which was compared to those of *hcp* Mg. According to their results, *hcp* Au has a shear modulus similar to that of *hcp* Mg, but a significantly higher (approximately four times higher) B value compared with that of *hcp* Mg. Therefore, to obtain deformable but tough *hcp* structured materials, a fabrication and stabilizing process needs to be established for *hcp* Au.

4. Conclusions

In conclusion, we observed the brittle fracture phenomenon of gold, one of the most ductile metals, under vertical loads by nanoindentation. This can be attributed to the simultaneous or complementary occurrence of the energy dissipation mechanisms, namely crack tip cleavage and dislocation nucleation, and the local phase transformation caused by external loads. It is unique compared to the other materials such as MoS_2 [44], $MoSe_2$ [45] or graphene [9,10] that maintain their crystal structure during fracture. In the case of materials like MoS_2 and $MoSe_2$, the presence of point defects, and in the case of graphene, the influence of defect density, can be said to be the causes of their brittle fracture behavior. On the other hand, Au nanosheets exhibit a more complex crack propagation pattern influenced by localized phase changes and structural defects. Our findings bear similarities to the dislocation-confinement-induced brittle behavior in layered systems reported by Hsia et al. [46], further supporting the idea that dimensional confinement can drastically alter fracture modes.

An interesting phenomenon was observed in which cracks due to brittle fracture propagate in three directions at an angle of 120°. Although a slightly different fracture pattern was shown depending on the type of nanoindenter tip, it was confirmed that a 120° radial fracture pattern was maintained, which is described in Table S1. The fracture pattern has been replicated in an MD simulation based on the crystalline structure, which supports the mechanism explaining the brittle fracture of the gold nanosheet as proposed in this study.

The Au nanosheet used in this study is not a perfect 2D material like graphene, so the approach from the references is not entirely applicable. However, it does show results that are considerably close. Also, the results from the MD simulation are based on the thickness of about 10 Au atoms, which is different from the actual thickness of the Au nanosheet used. Thus, it cannot be said that the interesting crack propagation phenomenon was perfectly reproduced, but it is significant in that it replicated the observed phenomenon. Moreover, this study suggests that even for materials with very high ductility, brittle fracture can begin due to the localized concentration of stress. Due to the brittle nature of the Au nanosheet, the indentation depth had to be limited to prevent fracture when evaluating the elastic properties. As a result, the fitting was performed within the elastic regime, where the deformation may be predominantly governed by prestress and the sensitivity to the Young's modulus relatively low. Nevertheless, we believe the extracted values still provide meaningful estimates of the elastic properties.

In the recent study by Ma et al. [47], it was demonstrated that the mechanical properties related to crystal size remain valid at the nanoscale. However, a distinct difference is observed between bulk gold composed of nanocrystals and gold at nanoscale thickness, which is ultimately attributed to the effects of dimensionality. This aligns closely with the claims made in the present study.

CRediT authorship contribution statement

Yoo Dayoung: Methodology, Formal analysis, Data curation. **Yang Cheol-Woong:** Methodology, Investigation, Formal analysis, Data curation. **Jang Joonkyung:** Software, Methodology, Investigation, Data curation. **Kim Tae-Hoon:** Methodology, Investigation, Data curation. **Kim Jong-Man:** Methodology, Investigation, Formal analysis, Data curation. **Kysar Jeffrey:** Writing – review & editing, Validation, Resources, Data curation, Conceptualization. **Lee Dongyun:** Writing – review & editing, Writing – original draft, Resources, Investigation, Formal analysis, Conceptualization. **Choi Yoon Suk:** Visualization, Software, Formal analysis. **Lim Byunkwon:** Writing – review & editing, Validation, Investigation, Formal analysis, Conceptualization. **Park Jieun:** Writing – original draft, Methodology, Investigation, Formal analysis, Data curation. **Lim Guh-Hwan:** Methodology, Formal analysis, Data curation.

Declaration of Generative AI and AI-assisted technologies in the writing process

During the preparation of this work the author(s) used ChatGPT-4 in order to improve grammar and language. After using this tool/service, the author(s) reviewed and edited the content as needed and take(s) full responsibility for the content of the publication.

Declaration of Competing Interest

The authors declare that they have no known competing financial interests or personal relationships that could have appeared to influence the work reported in this paper.

Acknowledgments

This research was funded by 1) the National Research Foundation of Korea (NRF) funded by the Ministry of Science and ICT (No. 2021R1F1A1054803); 2) the Center for Advanced Soft Electronics (CASE) under the Global Frontier Research Program (2013M3A6A5073177) through the National Research Foundation (NRF) funded by the Ministry of Science, ICT, and Future Planning. J.J. acknowledges the support by the Korea Planning & Evaluation Institute of Industrial Technology and fund by the Korean government (Ministry of Trade, Industry, and Energy, Ministry of Science and ICT, Ministry of the Interior and Safety, National Fire Agency, Project Title:

Development of gas hydrate extinguishing agent and fire suppression technology for inaccessible fires, Project Number: 2760000002).

Appendix A. Supporting information

Supplementary data associated with this article can be found in the online version at doi:10.1016/j.eml.2025.102323.

Data Availability

Data will be made available on request.

References

[1] C. Li, W. Cai, B. Cao, F. Sun, Y. Li, C. Kan, L. Zhang, Adv. Funct. Mater. 16 (2006) 83–90.
[2] Y. Shao, Y. Jin, S. Dong, Chem. Commun. (9) (2004) 1104–1105.
[3] D. Ibano, Y. Yokota, T. Tominaga, Chem. Lett. 32 (2003) 574–575.
[4] G.D. Moon, G. Lim, J.H. Song, M. Shin, T. Yu, B. Lim, U. Jeong, Adv. Mater. 25 (2013) 2707–2712.
[5] G. Lim, N. Lee, B. Lim, J. Mater. Chem. C. 4 (2016) 5642–5647.
[6] K.H. Kim, B. Kumar, K.Y. Lee, H.-K. Park, J.-H. Lee, H.H. Lee, H. Jun, D. Lee, S.-W. Kim, Sci. Rep. 3 (2013) 2017.
[7] Y. Lu, J. Song, J.Y. Huang, J. Lou, Adv. Funct. Mater. 21 (2011) 3982–3989.
[8] C. Wang, H. Wang, T. Huang, X. Xue, F. Qiu, Q. Jiang, Sci. Rep. 5 (2015) 10213.
[9] C. Lee, X. Wei, J.W. Kysar, J. Hone, Science 321 (2008) 385–388.
[10] G.-H. Lee, R.C. Cooper, S.J. An, S. Lee, A. van der Zande, N. Petrone, A. G. Hammerberg, C. Lee, B. Crawford, W.C. Oliver, J.W. Kysar, J. Hone, Science 340 (2013) 1073–1076.
[11] C. Cao, Y. Sun, T. Filleter, J. Mater. Res. 29 (2014) 338–347.
[12] T.H. Wang, T.-H. Fang, S.-H. Kang, Y.-C. Lin, Nanotechnology 18 (2007) 135701.
[13] J.W. Kysar, J. Mech. Phys. Solids 51 (2003) 795–824.
[14] J.W. Kysar, in: H. Kitagawa, Y. Shibutani (Eds.), IUTAM Symposium on Mesoscopic Dynamics of Fracture Process and Materials Strength. Solid Mechanics and its Applications, Springer, Dordrecht, 2003, p. 115.
[15] C. Deng, F. Sansoz, Nano Lett. 9 (2009) 1517–1522.
[16] M.J. Lagos, F. Sato, D.S. Galvão, D. Ugarte, Phys. Rev. Lett. 106 (2011) 055501.
[17] J. Song, D.J. Srolovitz, Scr. Mater. 57 (2007) 885–888.
[18] J. Song, D.J. Srolovitz, Acta Mater. 55 (2007) 4759–4768.
[19] X. Huang, S. Li, Y. Huang, S. Wu, X. Zhou, S. Li, C.L. Gan, F. Boey, C.A. Mirkin, H. Zhang, Nat. Commun. 2 (2011) 292.
[20] S. Nosé, A unified formulation of the constant temperature molecular dynamics methods, J. Chem. Phys. 81 (1984) 511–519.
[21] W.G. Hoover, Canonical dynamics: Equilibrium phase-space distributions, Phys. Rev. A 31 (1985) 1695–1697.
[22] A.P. Thompson, H.M. Aktulga, R. Berger, D.S. Bolintineanu, W.M. Brown, P. S. Crozier, P.J. in 't Veld, A. Kohlmeyer, S.G. Moore, T.D. Nguyen, R. Shan, M. J. Stevens, J. Tranchida, C. Trott, S.J. Plimpton, LAMMPS - a flexible simulation tool for particle-based materials modeling at the atomic, meso, and continuum scales, Comput. Phys. Commun. 271 (2022) 108171.
[23] W. Humphrey, A. Dalke, K. Schulten, VMD: Visual molecular dynamics, J. Mol. Graph 14 (1996) 33–38.
[24] E.R. Jette, F. Foote, J. Chem. Phys. 3 (1935) 605–616.
[25] Y. Wang, S. Curtarolo, C. Jiang, R. Arroyave, T. Wang, G. Ceder, L.-Q. Chen, Z.-K. Liu, Calphad 28 (2004) 79–90.
[26] V. Germain, J. Li, D. Ingert, Z.L. Wang, M.P. Pileni, J. Phys. Chem. B. 107 (2003) 8717–8720.
[27] C. Cayron, M.D. Hertog, L. Latu-Romain, C. Mouchet, C. Secouard, J. Rouviere, E. Rouvierea, J. Simonatoa, J. Appl. Cryst. 42 (2009) 242–252.
[28] R. Jin, Science 294 (2001) 1901–1903.
[29] N. Vandenberghe, R. Vermorel, E. Villermaux, Phys. Rev. Lett. 110 (2013) 174302.
[30] Q. Ding, H. Bei, X. Wei, Y.F. Gao, Z. Zhang, Mater. Today Nano 14 (2021) 100110.
[31] Q. Ding, Y. Li, J. Ouyang, X. Wei, Z. Zhang, Y.F. Gao, H. Bei, Mater. Today Nano 24 (2023) 100407.
[32] J.R. Rice, R. Thomson, Philos. Mag. 29 (1) (1974) 73–97.
[33] J. Diao, K. Gall, M.L. Dunn, Nat. Mater. 2 (2003) 656–660.
[34] U. Komaragiri, M.R. Begley, J.G. Simmonds, J. Appl. Mech. 72 (2005) 203–212.
[35] K.T. Wan, S. Guo, D.A. Dillard, Thin Solid Films 425 (2003) 150–162.
[36] J.R. Davis. Metals Handbook Desk Edition, second ed., CRC press, 1998.
[37] Z. Dai, N. Lu, J. Mech. Phys. Solids 149 (2021) 104320.
[38] T.G.J. Chandler, D. Vella, J. Mech. Phys. Solids 144 (2020) 104109.
[39] N. Bhatia, W. Nachbar, Int. J. Non-Linear Mech. 3 (1968) 307–324.
[40] M.R. Begley, T.J. Mackin, J. Mech. Phys. Solids 52 (2004) 2005–2013.
[41] G. Simmons, H. Wang, MIT Press, Cambridge, MA, 1971.
[42] A. Reuss, Z. Angew. Math. Mech. 9 (1929) 49–58.
[43] R. Hill, Proc. Phys. Soc. Lond., Sect. A 65 (1952) 349–354.
[44] G. Wang, Y.-P. Wang, S. Li, Q. Yang, D. Li, S.T. Pantelides, J. Lin, Adv. Sci. 9 (2022) 2200700.
[45] Y. Yang, X. Li, M. Wen, E. Hacopian, W. Chen, Y. Gong, J. Zhang, B. Li, W. Zhou, P. M. Ajayan, Q. Chen, T. Zhu, J. Lou, Adv. Mater. 29 (2017) 1604201.
[46] K.J. Hsia, S. Zhigang, Y. Wei, J. Mech. Phys. Solids 42 (1994) 877–896.
[47] L. Ma, L. Du, S. Wang, Q. Wang, S. Xue, H. Zhu, Q. Liu, Nano Res 16 (2023) 13400–13408.